coatings

MDPI

Article

The Effect of Nb on the Microstructure and High-Temperature Properties of Co-Ti-V Superalloys

Pengjie Zhou [1], Shenfa Ni [1], Kunjie Luo [2,*], Wanxiang Zhao [2], Enze Liu [3], Yanxin Qiao [1,*] and Shujin Chen [1]

[1] School of Materials Science and Engineering, Jiangsu University of Science and Technology, Zhenjiang 212000, China; zhoupengjie@just.edu.cn (P.Z.)
[2] Suzhou Nuclear Power Research Institute, Suzhou 215004, China
[3] Institute Metal Research, Chinese Academy of Sciences, Shenyang 110016, China
* Correspondence: luokunjie007@163.com (K.L.); yxqiao@just.edu.cn (Y.Q.)

Abstract: The effect of Nb on the microstructure evolution of the γ' phase in Co-Ti-V alloys has been studied. The yield strength and ultimate strength of the alloys are measured via compression at 900 °C. This indicates that the alloys with 1% at. Nb present a dual γ and γ' microstructure. A Co_3V phase exists in 2Nb and 3Nb alloys. The mismatch increases with the increment in Nb content. The yield strength of the alloys rises as the Nb addition increases. After compression at 900 °C, the <101>-type dislocation causes shearing of the γ' phase in the plane of the base alloy. In the 1Nb alloy, the $< 1\bar{1}0>$-type dislocation reacts at the γ/γ' interface to generate $1/3<1\bar{2}1>$ super-partial dislocation, and then the γ' phase is cut by this dislocation and stacking faults are formed.

Keywords: Co-Ti-V alloys; lattice misfit; high-temperature deformation; dislocations

1. Introduction

Superalloys are alloys based on nickel, iron–nickel, and cobalt, and are widely employed at temperatures of 540 °C and above. They are widely applied in parts working at elevated temperatures, for instance, aircraft blade, petrochemical equipment, and chemical plant equipment. Recently, they have been used in the automotive industry as materials for turbines. Up to now, nickel-based superalloys have been the most popular in those fields [1].

In 2006, a γ'-Co_3 (Al,W) precipitate which is capable of being stabilized at 900 °C with an $L1_2$ structure was reported by Ishida et al. [2]. Compared with Ni-based superalloys, the melting point of Co is higher than that of Ni by about 40 °C, and conventional Co-based alloys have excellent corrosion resistance and weldability [3], promoting their superiority to the Ni-based superalloy in some applications. Because of the lack of a stable γ' precipitate-strengthening effect, the traditional Co-based superalloy shows inferior strength to that of the Ni-based γ' hardening alloys when operating at elevated temperatures [4,5]. The new discovery of Co_3 (Al,W)- γ' opened up new pathways to developing Co-based alloys with superior high-temperature strength. However, it has been demonstrated that the γ'-Co_3 (Al,W) precipitate is not stable when the temperature is over 1000 °C, so the existing temperature of the γ' is far lower than that of the Ni-based superalloy, indicating its poor high-temperature stability [6]. Increasing the W content can stabilize the strengthening phase, but the higher content of W will increase the mass density and limit the application of such alloys [7–10]. It is necessary to search for a light element to replace W and to ensure the phase stability of the hardening precipitate.

check for updates

Academic Editor: Vincent Ji

Received: 26 November 2024
Revised: 27 December 2024
Accepted: 2 January 2025
Published: 6 January 2025

Citation: Zhou, P.; Ni, S.; Luo, K.; Zhao, W.; Liu, E.; Qiao, Y.; Chen, S. The Effect of Nb on the Microstructure and High-Temperature Properties of Co-Ti-V Superalloys. *Coatings* **2025**, *15*, 53. https://doi.org/10.3390/coatings15010053

Copyright: © 2025 by the authors. Licensee MDPI, Basel, Switzerland. This article is an open access article distributed under the terms and conditions of the Creative Commons Attribution (CC BY) license (https://creativecommons.org/licenses/by/4.0/).

Among those Co-based alloys that have been reported so far, only the γ'-Co_3Ti phase with an $L1_2$ structure has been found to be stable. However, it presents large lattice mismatch, which can affect the properties of the alloy [11]. Liu et al. point out that the alloying of V to the Co-Ti binary system would reduce the mismatch between the dual γ/γ' phases and improve the high-temperature stability of the alloys [12]. It is reported that V, Sc, Y, Cr, Zr, Mo, Ta, Nb, Hf, and W tend to occupy the Ti site in the lattice and degrade the structural stability of $L1_2$-Co_3Ti. In 2014, Liu and Ruan discovered the existence of a stable γ-γ' dual-phase section in a Co-Ti-V ternary alloy at 900 °C [13]. After that, a novel Co-Ti-V ternary alloy was developed which possesses the following advantages compared to Co-Al-W alloys: low density, high γ' solvus temperature, and superior strength at elevated temperatures [14]. The phase equilibria of ternary Co-Ti-V at 873 K was investigated by Zhou [15], and the interdiffusion coefficients of the elements were studied by Zhang, showing that Ti diffuses faster than V [16]. Verma et. al. illustrated that V decreases the solvus temperature of γ', and it modifies the mismatch between γ and γ' from positive to negative [17]. Ni and Al additions were reported to increase the volume fraction and stability of the γ' precipitate [18,19]. Ni is demonstrated to reduce the solvus temperature of γ' in Co-8Ti-11V alloys [19]. Ru seems to have no remarkable influence on the solvus temperature of γ', but modifies the portioning behaviors of Ti and V in the alloy, consequently enhancing the strength of the alloy [20]. Previous research indicates that Nb is a strong γ' former and increases the solvus temperature and volume fraction of the γ' phase; W has similar effect as Nb [21]. Nb is reported to slightly improve the resistance of alloys to hot corrosion, but is less effective than Mo and Ti [22], while Migas and Klein illustrated that Nb degrades the oxidation resistance of Co-Al-W alloys [23,24]. However, their research only covered the composition of Co-10V-4Ti-2Nb (at. %); more studies are necessary to explore the influence of Nb content on the microstructure and properties of Co-Ti-V alloys. This article aims to explore the influence of Nb on microstructure evolution and mechanical improvement and to gain the reliable addition range of Nb in the Co-Ti-V tertiary alloy.

In this work, five Co-6Ti-11V-xNb (x = 0, 0.5, 1, 2, 3) quaternary superalloys are designed, prepared by vacuum arc melting, and investigated. The effect of Nb content on the structure and mechanical properties of Co-Ti-V superalloys is investigated by using the below methods.

2. Materials and Methods

The nominal compositions of the target alloys used in this study are shown in Table 1, and for the convenience of presentation, these materials are abbreviated according to the Nb content in each alloy. High-purity cobalt (99.95%), V (99.95%), and Ti (99.9%) were adopted to prepare the target material. The alloy was firstly melted into ingots using a WK-II vacuum arc-melting furnace. In the melting process, the chamber was vacuumed to 0.1 bar first, then gassed with argon (99.999%); after repeatedly cleaning the atmosphere, the materials were arc-melted under argon atmosphere. The button-shaped sample was turned over and remelted more than 6 times to homogenize the composition of the entire ingot. Each ingot was approximately 70 g. Using this melting method, the cooling rate of the ingot was estimated to be 300 °C/s during the solidification process, and the secondary dendrite arms' spacing was 450 μm on average. The alloys were sealed in quartz capsules for homogenization treatment at 1100 °C for 48 h, then quenched in cold water. After that, the alloys were quartz-sealed again and aged at 870 °C for 72 h, and then cooled in air to room temperature. The specimen was electrolytically etched using 10 mL of HNO_3 plus 20 mL of CH_3COOH and 170 mL of distilled water with 6 V. The morphology of the γ' phase was observed by using a Zeiss–Merlin Compact Field Emission Scanning Electron

Microscope (FE-SEM) (Zeiss: Oberkochen, Germany) to calculate the size distribution and volume fraction of the γ' precipitates. The phase constitutes were observed by using a JEM-2100F Transmission Electron Microscope (TEM) (JEOL Ltd.: Tokyo, Japan), and the distribution of elements in the γ phase and γ' phase was investigated by Oxford Energy Disperse Spectroscopy (EDS) (Oxford Instruments: Abington, UK) with INCA T80 equipped with the TEM. The composition was averaged from ten points of 3 different regions. The evaluation of dislocation after deformation was performed. The film for the TEM analyses was obtained by using twin-jet electropolishing in a solution of 6% perchloric acid and methanol conducted at −30 °C with 25 V. Shimadzu XRD-6000 (Shimadzu: Kyoto, Japan) was employed to investigate the phase constitutes and analyze the lattice mismatch of the γ and γ' phases. Powders used in the XRD test were machined from bulk materials, then sealed in quartz, heated to 900 °C for 3 min, and furnace-cooled to room temperature. A scanning rate of 4°/min was used in the range of 20–90° to analyze the phases. A scanning speed of 1°/min was adopted to measure the mismatch in the interval between 47° and 55°. Origin Pro 9.1 was employed to fit the peak profiles and analyze the mismatch. The compression experiments were performed at a strain rate of $3 \times 10^{-4}s^{-1}$ and a ramping rate of 10 °C/s to 900 °C, using a Gleeble-3800 (Gleeble: Poestenkill, NY, USA) thermal simulator. When the temperature rose to 900 °C, it was maintained for 3 mins before loading. The strain rate used in the study was 3×10^{-4}/s, which was in the range of $\left(1 \times 10^{-4}/s \sim 1 \times 10^{-3}/s\right)$ that is widely adopted by previous research [25,26]. The stress corresponding to a 0.2% offset strain was taken as the yield strength. After high-temperature compression, the specimens were water-quenched.

Table 1. Compositions of investigated alloys (at. %).

Alloy	Nominal Composition (at.%)			
	Co	Ti	V	Nb
Base	Bal	6	11	-
0.5 Nb	Bal	6	11	0.5
1 Nb	Bal	6	11	1
2 Nb	Bal	6	11	2
3 Nb	Bal	6	11	3

3. Results and Discussion

3.1. Microstructure of Alloys with Varied Nb Content

Figure 1 shows the XRD patterns of the alloys with varied Nb content. The patterns of the 0Nb, 0.5Nb, and 1Nb alloys are similar, with three relatively obvious peaks which are actually composed of the matrix (γ) and the strengthening precipitate (γ'). The other peaks in the 2Nb and 3Nb alloys indicate the precipitation of Co_3V.

Figure 2 shows the microstructure of the alloys. The 0Nb, 0.5Nb, and 1Nb alloys have no other precipitates except the γ and γ' phases (Figure 2a–c). Meanwhile, the 2Nb and 3Nb alloys exhibit a needle-like precipitate which corresponds to the Co_3V phase in the XRD pattern. The selected area electron diffraction (SAED) of this phase was conducted (Figure 3). The phase was identified as Co_3V by XRD as well as EDS analysis of the TEM and electron diffraction patterns. Therefore, the Nb addition leads to the formation of an x phase (D019) if its content exceeds 1% (at. %). The volume fractions of the x-Co_3V phase in the 2Nb and 3Nb alloys are 14.04% and 37.54, respectively.

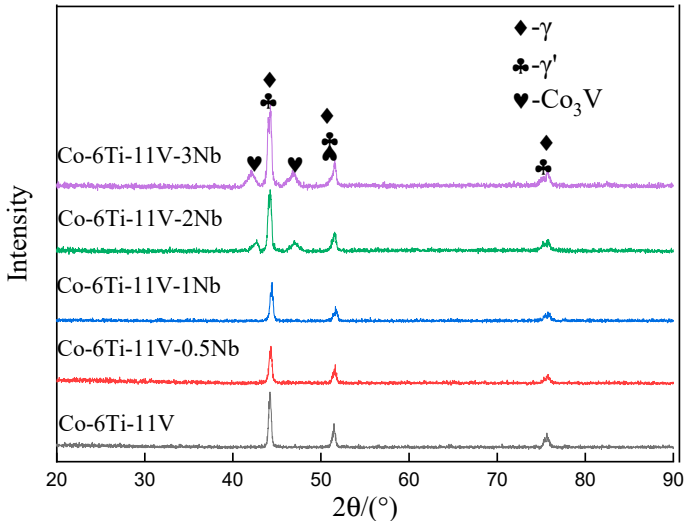


Figure 1. XRD analysis of alloys with various Nb contents.

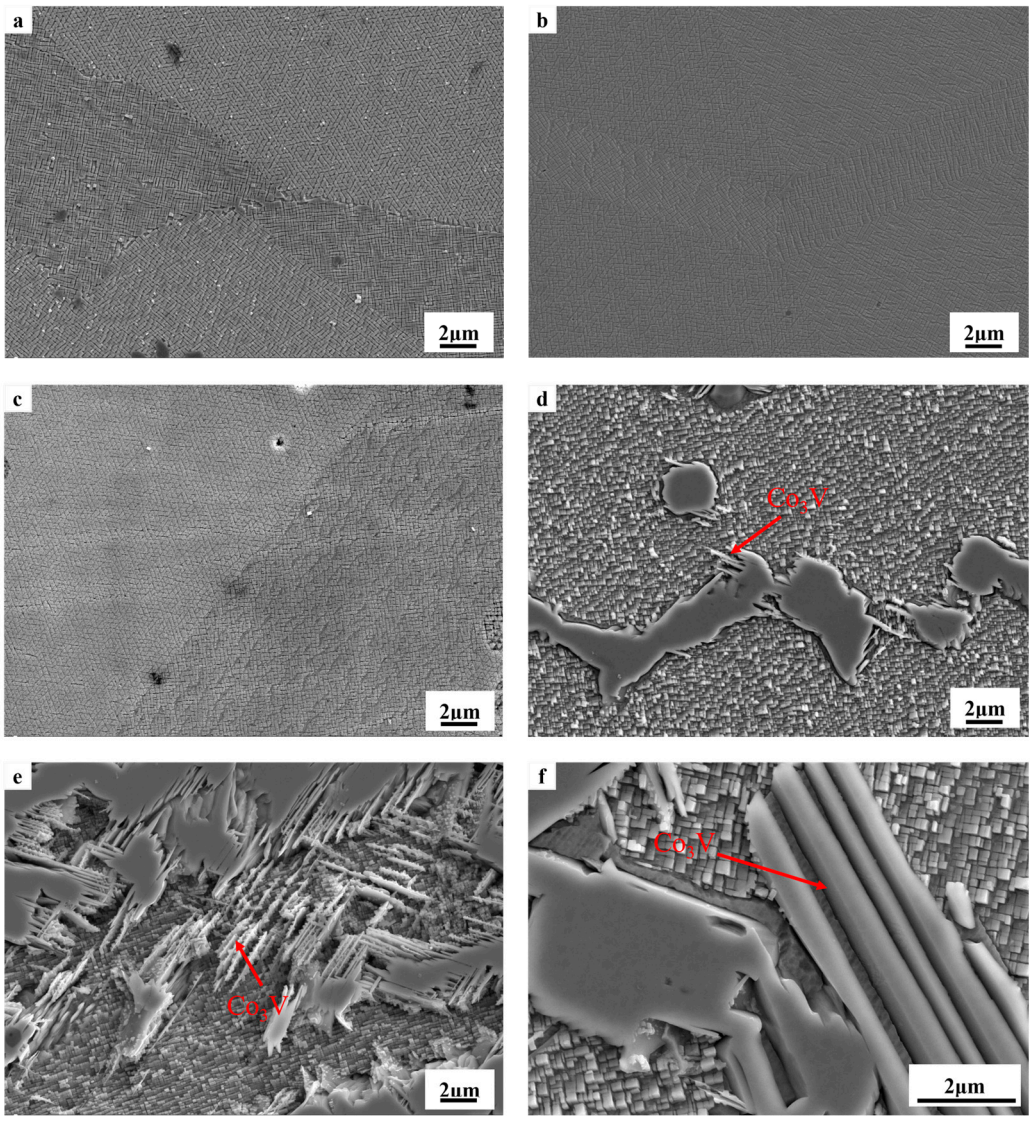


Figure 2. Microstructure of alloys with varied Nb content: (**a**) Nb-free; (**b**) 0.5Nb; (**c**) 1Nb; (**d**) 2Nb; (**e**) 3Nb; (**f**) details of Co_3V phase in 2Nb alloys.

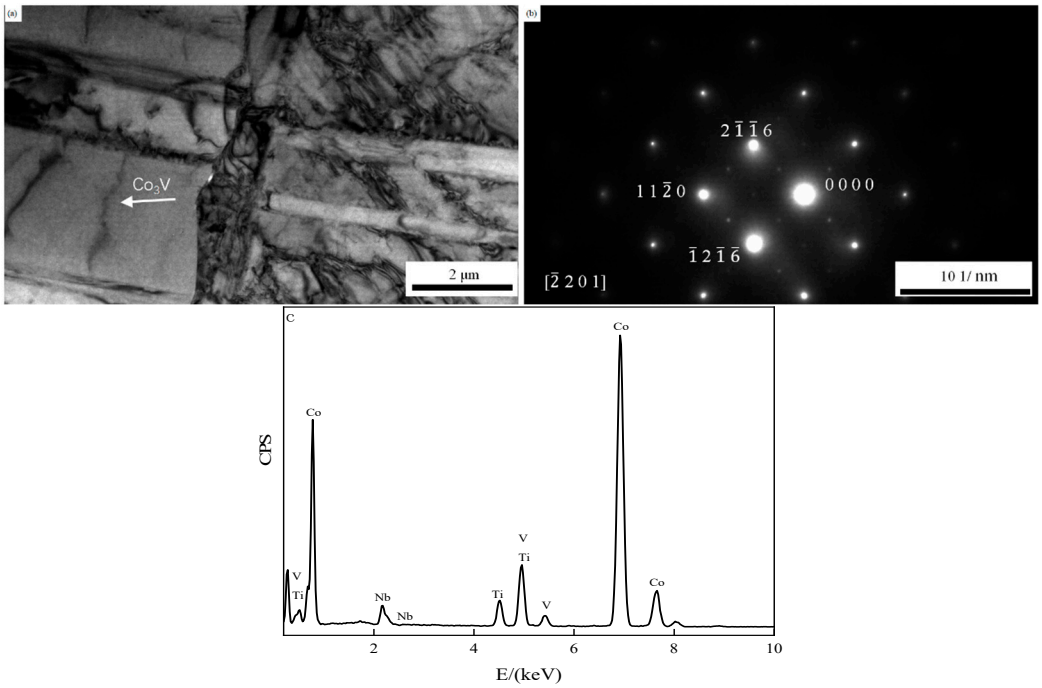


Figure 3. (**a**) TEM image of Co_3V phase; (**b**) selected area electron diffraction pattern of Co_3V phase; (**c**) EDS pattern of Co_3V phase.

3.2. Lattice Mismatch Between γ/γ′ Phases

Since the γ/γ' phases have similar lattice constants, the observed (002) peaks are doublets due to the overlap from both peaks of the dual phases. Figure 4 shows the separation peaks of the γ phase and the γ' phase and the fitted curves obtained corresponding to the (200) crystal plane. The equations for calculating the lattice constant and mismatch are as follows:

$$\alpha = \frac{\lambda}{2\sin\theta}\sqrt{H^2+K^2+L^2} \quad (1)$$

$$\delta = \frac{2(\alpha_{\gamma\prime} - \alpha_{\gamma})}{\alpha_{\gamma\prime}+\alpha_{\gamma}} \times 100\% \quad (2)$$

where α is the lattice parameter of the corresponding phase; θ represents the diffraction angle (°); λ is the wavelength of incident X-rays (Å); H, K, and L are the specific plane indexes; α_{γ} is the lattice constant of the γ phase (Å); $\alpha_{\gamma\prime}$ stands for the lattice constant of the γ' phase (Å); δ is defined as the γ/γ' two-phase lattice mismatch (%). The lattice constants of the γ phase and the γ' phase of alloys with various Nb contents are shown in Table 2, and the calculated lattice mismatches were given as well. According to these data, the lattice mismatch gradually rises with the increase in Nb content.

Table 2. Lattice constants of γ and γ' phases and lattice mismatch between dual phases in alloys with various Nb contents.

Alloy (at. %)	γ'-Phase Lattice Constant α_{γ}/Å	γ-Phase Lattice Constant α_{γ}/Å	Lattice Mismatch δ/%
0Nb	0.3594	0.3567	0.76
0.5Nb	0.360	0.357	0.81
1Nb	0.359	0.356	0.82
2Nb	0.3597	0.357	0.85
3Nb	0.3595	0.3564	0.86

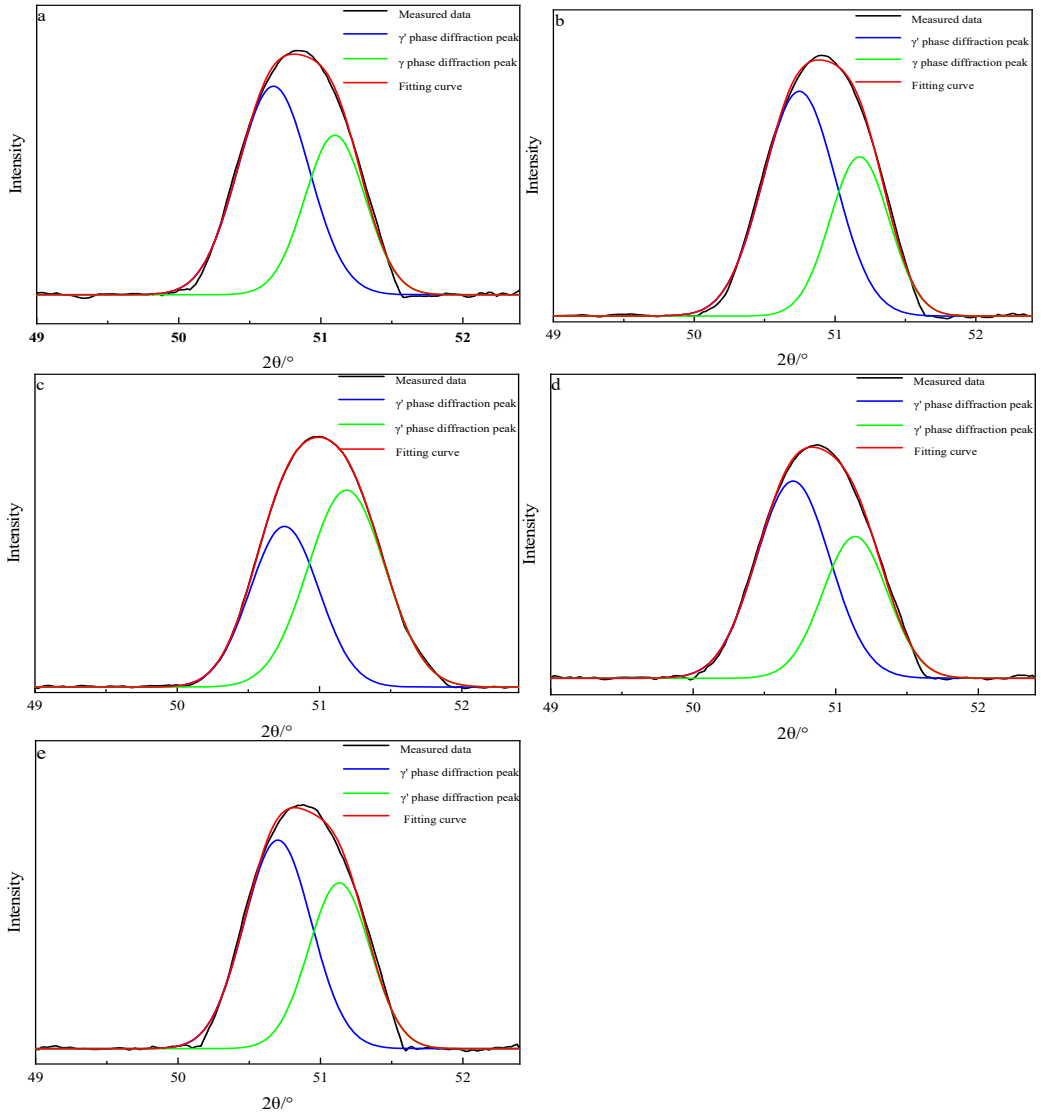


Figure 4. XRD peak-differentiating and -imitating profiles of alloys with varied Nb content: (**a**) Nb-free; (**b**) 0.5Nb; (**c**) 1Nb; (**d**) 2Nb; (**e**) 3Nb.

3.3. γ′-Phase Morphologies of Alloys with Varied Nb Content

Figure 5 shows the γ′ morphologies in the alloys with varied Nb content. The γ′ phase is relatively uniformly arranged, and all of them are cuboidal in shape (Figure 5a–c). As illustrated in Figure 5d, when the Nb content increases to 2 at. %, the γ-matrix channel is thin, and the size of the γ′ precipitate varies and drops significantly, but it remains cuboidal in shape. Figure 5e shows the extremely regular shape of the γ′ phase, with a wide range of sizes.

The average size and volume ratio of the γ′ phase in the five materials are shown in Table 3. The volume ratios of the γ′ phase in the 2Nb and 3Nb alloys were not investigated because of the presence of a large amount the Co_3V phase in the two alloys. Since mass precipitation of x–Co_3V will greatly degrade the ductility of the alloys, it is meaningless to analyze the volume ratio of the γ′ phase in the 2Nb and 3Nb alloys. The average size of the γ′ phase increases and then decreases with the rise in Nb content, which peaks at 0.5Nb. With the increased Nb content, the volume ratio of the γ′ phase increases, and the volume fraction of the γ′ phase in the 1Nb alloy reaches the maximum, at 84.7%.

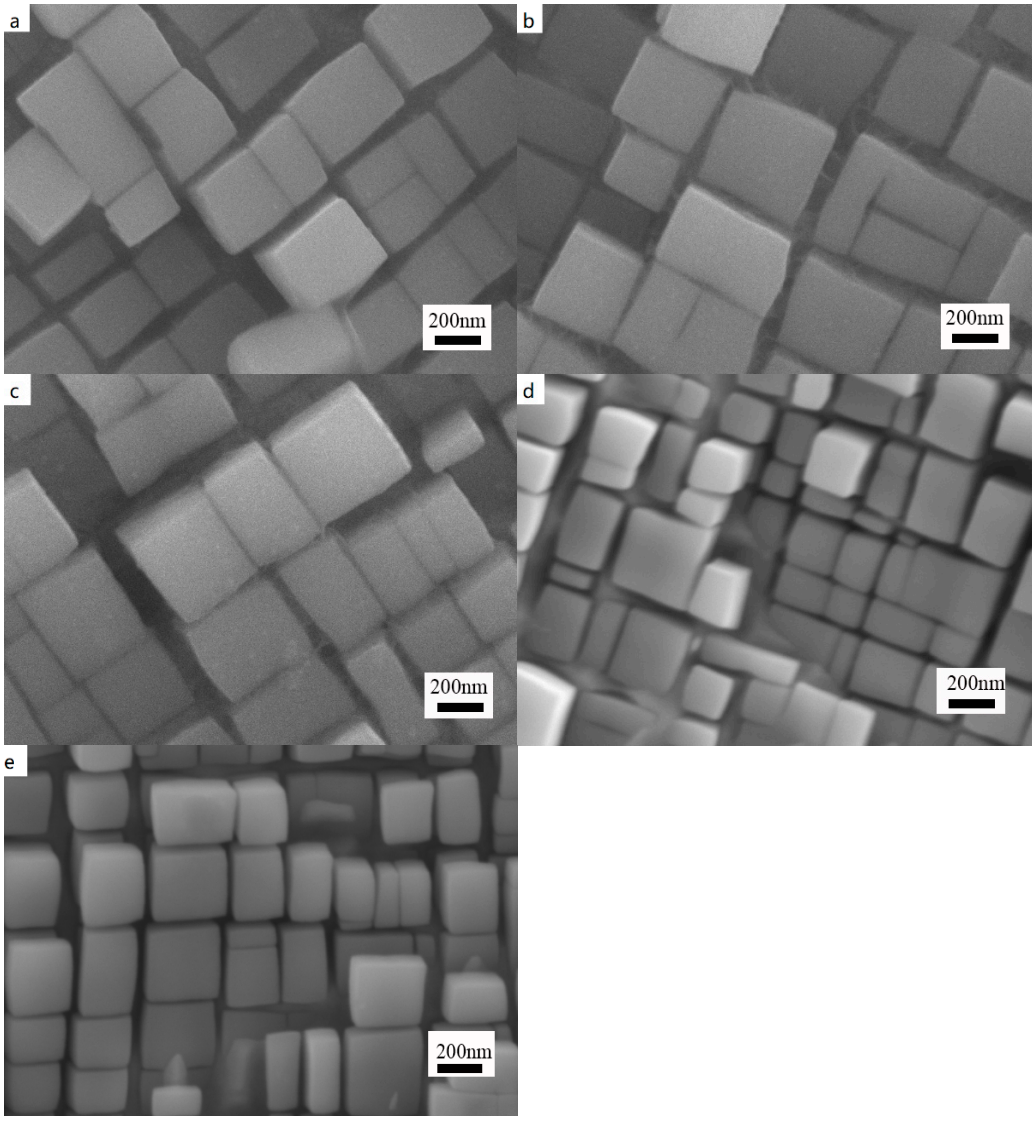


Figure 5. γ'-phase morphology of alloys with different Nb contents: (**a**) Nb-free; (**b**) 0.5Nb; (**c**) 1Nb; (**d**) 2Nb; (**e**) 3Nb.

Table 3. Average size and volume ratios of γ' phase of each alloy.

Alloy	Average Size (nm)	Volume Fraction (%)
0Nb	222.2	84.3
0.5Nb	303.9	84.4
1Nb	252.4	84.7
2Nb	191.0	-
3Nb	189.0	-

3.4. Distribution of Alloying Elements in γ Phase and γ' Phase

Analysis of the elemental distribution behavior in the γ and γ' phases of the alloys was conducted by EDS equipped with a TEM, which was conducted in a STEM model. The expression of the elemental distribution coefficient (K_X) is as follows:

$$K_x = C_{\gamma\prime-x}/C_{\gamma-x} \quad (3)$$

where $C_{\gamma\prime-x}$ represents the atomic percent of element X in the γ' precipitate (at. %), and $C_{\gamma-x}$ is the atomic percent of element X in the γ channel (at. %). Table 4 lists the

compositions of the γ phase and the γ′ phase in the alloys, and the partitioning coefficients of each elements in the alloys are shown in Figure 6. The partitioning coefficients of Ti and Nb are always greater than 1, and they partition preferentially to the γ′ precipitate. Furthermore, the partitioning coefficient of Ti increases with the rise in Nb additions, as Nb promotes the enrichment of Ti into the γ′ phase. The partition coefficients of V in the 0Nb, 0.5Nb, and 1Nb alloys fluctuate near 1; as the Nb content continues to increase, the partitioning coefficient of V rises gradually. These results show that the addition of Nb leads to Ti and V enrichment in the γ′ matrix rather than in the γ matrix, and consequently, Nb addition results in the rise in the γ′ volume fraction in the alloys.

Table 4. The elemental components of the γ phase and the γ′ phase in the alloys with varied Nb content.

Alloy		Composition (at. %)			
		Co	Ti	V	Nb
Co6Ti11V	γ	81	6	13	-
	γ′	79.9	7.1	13	-
Co6Ti11V0.5Nb	γ	78.4	6.9	14.1	0.6
	γ′	78.4	7.4	13.5	0.7
Co6Ti11V1Nb	γ	81.2	4.7	13.4	0.8
	γ′	78.6	6.7	13.4	1.4
Co6Ti11V2Nb	γ	85.5	3.3	10.2	1.1
	γ′	79.3	5.8	12.8	2.1
Co6Ti11V3Nb	γ	86.4	2.5	10.1	1.1
	γ′	76.6	6.1	14.1	3.4

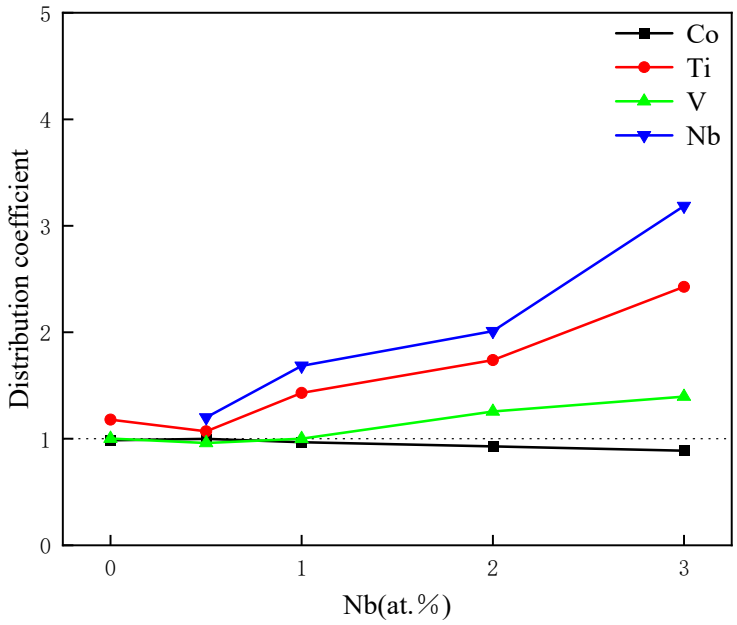


Figure 6. Partitioning coefficients of elements in γ and γ′ phases in alloys with various Nb contents.

3.5. Strength at Elevated Temperature

The 0.2-percent offset yield strength of alloys subjected to compression tests at 900 °C is shown in Table 5. The yield strength rises gradually with the increasing Nb content. The 3Nb alloy possesses the highest yield strength at 900 °C, which is 496 MPa, while the 0Nb alloy has the lowest yield strength, which can be related to the lowest γ' volume fraction in the 0Nb alloy. The alloying of Nb can enhance the tensile properties of alloys with proper additions. As listed in Table 5, the yield strength of the 1Nb alloy is higher than that of the conventional Co-based superalloy (Haynes188) and the newly developed Co-9Al-W alloys. However, it is lower than that of the precipitate-hardening Ni-based superalloy (In939).

Table 5. Yield strength at 900 °C of alloys with different Nb contents.

Alloy	Yield Strength (MPa)
Co-6Ti-11V	323
Co-6Ti-11V-0.5Nb	351
Co-6Ti-11V-1Nb	391
Co-6Ti-11V-2Nb	404
Co-6Ti-11V-3Nb	496
Hayness	280 [6]
Mar-M247	392 [6]
In939	520 [18]
Mar-M302	361 [18]
Co9Al9W	263 [27]

3.6. The γ'-Phase Morphologies of Alloys After Compression at 900 °C

The morphologies of the γ' precipitate of the 0Nb, 0.5Nb, and 1Nb alloys after compression at 900 °C are shown in Figure 7, and the average size as well as the volume ratios of the γ' particles in each alloy are listed in Table 6. The γ' precipitate in the 0Nb alloy is not uniformly arranged, and the mean size of the γ' particle increases from 222.2 nm to 271.7 nm compared with before compression. The γ' precipitate in the 0.5Nb alloy is much the same as that before deformation. The γ-matrix channel in the 1Nb alloy is extremely narrow, and the mean size of the γ' particle is only slightly increased in comparison with before compression. The volume fraction of the γ' particle in the 0Nb, 0.5Nb, and 1Nb alloys is substantially smaller than that before the test. This may be due to the fact that parts of the γ' phases were dissolved with load during the hot compression process. During deformation at elevated temperatures, γ' is repeatedly cut by dislocations, especially in the interface of γ' and γ, and some mini γ' particles may be generated by cutting the large γ' particles. And the mini γ' particles dissolve during the compression test. In contrast, the 1Nb alloy achieves the minimal particle size increase and the lowest volume fraction reduction. These results show that the correct addition of Nb is beneficial for improving the phase stability of alloys. Previous research has reported that Nb improves the phase stability of γ' phases in Co-based superalloys [6,21,25].

Table 6. Average dimensions and volume fractions of particles of each alloy after compression at 900 °C.

Alloy	Average Size (nm)	Volume Fraction (%)
Co-6Ti-11V	271.7	58.5
Co-6Ti-11V-0.5Nb	302.1	48.4
Co-6Ti-11V-1Nb	264.4	65.9

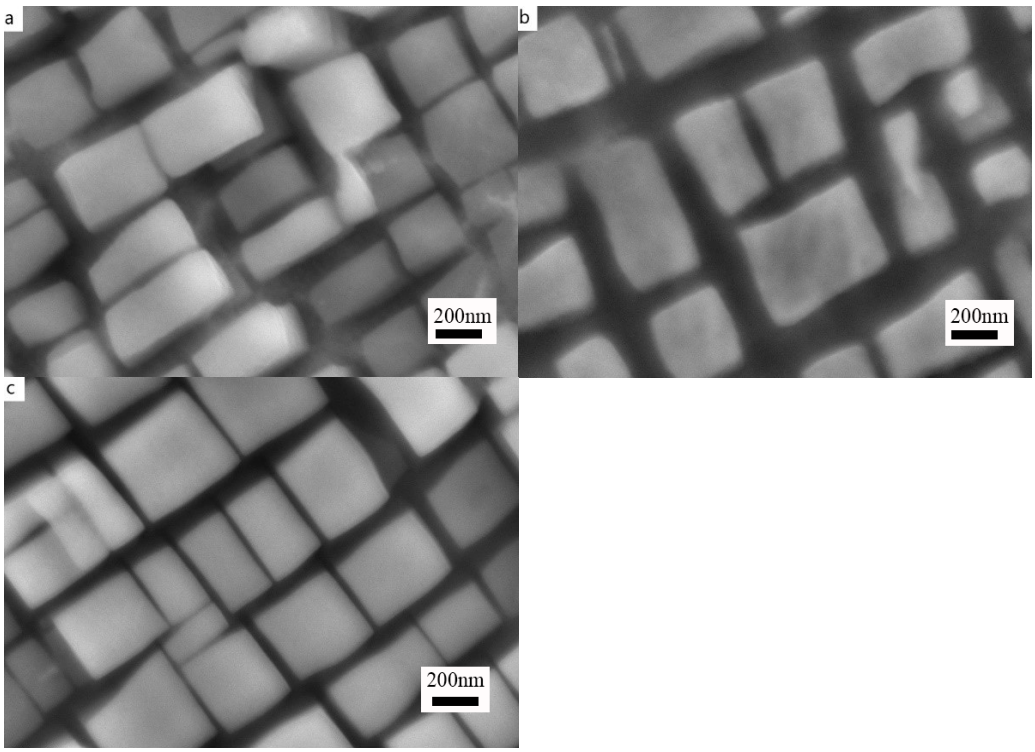


Figure 7. The γ′ morphologies after compression at 900 °C: (**a**) 0Nb; (**b**) 0.5Nb; (**c**) 1Nb.

3.7. Deformation Behavior of Alloys

Figure 8 shows the dislocation configurations of the Co6Ti11V alloy after the compression test at 900 °C. In Figure 8a, a dense dislocation distribution in the γ′ phase is observed, indicating that dislocation sliding is the primary deformation mechanism in the γ′ precipitate. And shearing of the γ′ precipitate by pair dislocations is evident. When imaged with g = $0\overline{2}\overline{2}$, the dislocation A is observed in Figure 8a, while imaging with g = $2\overline{2}\overline{2}$ reveals that the dislocation A is invisible, as shown in Figure 8b; thus, it can be roughly judged that the Berger vector of the dislocation A is b = [101], and this type of dislocation causes shearing of the γ′ phase in the {111} plane.

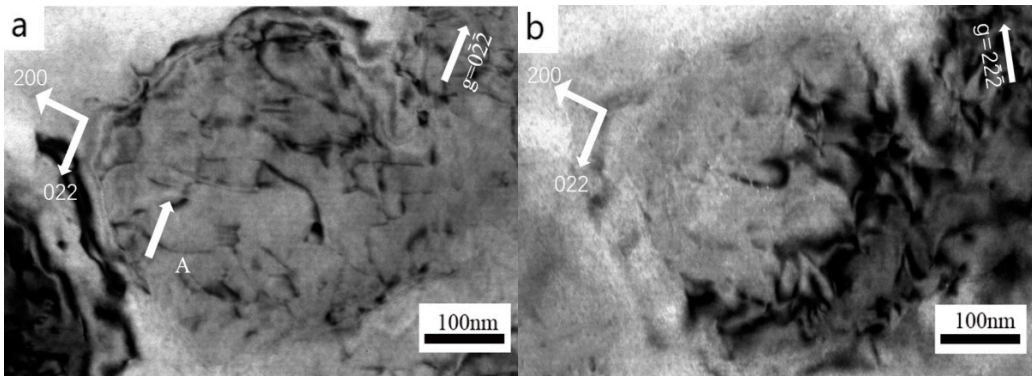


Figure 8. Dislocation configuration of 0Nb alloy after compression: (**a**) g = $0\overline{2}\overline{2}$; (**b**) g = $2\overline{2}\overline{2}$.

A series of typical TEM images of the Co6Ti11V1Nb alloy after compression at 900 °C is shown in Figure 9. As illustrated in Figure 9a, numerous dislocations are visible in the γ′ phase when imaged with g = $\overline{2}\overline{2}0$. In contrast, when imaged with g = 220, as shown in Figure 9b, there is a high density of dislocations visible in the γ channel, and a few dislocations in the γ′ phase are observed. As illustrated in Figure 9c, dense dislocations are observed in the γ′ phases when imaged with g = $\overline{1}11$, whereas the dislocations in the

γ channel are invisable. When imaged with g = $\bar{1}3\bar{1}$, the dislocations in the γ channel are visible, while the dislocations in the γ′ phases are invisible, which is revealed in Figure 9d. Figure 9c shows that a stacking fault A and dislocation B are observed; based on Figure 9a,d, the type of stacking fault A can be determined to be R (displacement vector) = [$1\bar{1}2$]. According to Figure 9a,b, the Berger vector b = [$1\bar{1}0$] of the dislocation B can be determined. According to Equation (4), it can be seen that the superlattice intrinsic fault A is a result of the reaction of the dislocation B.

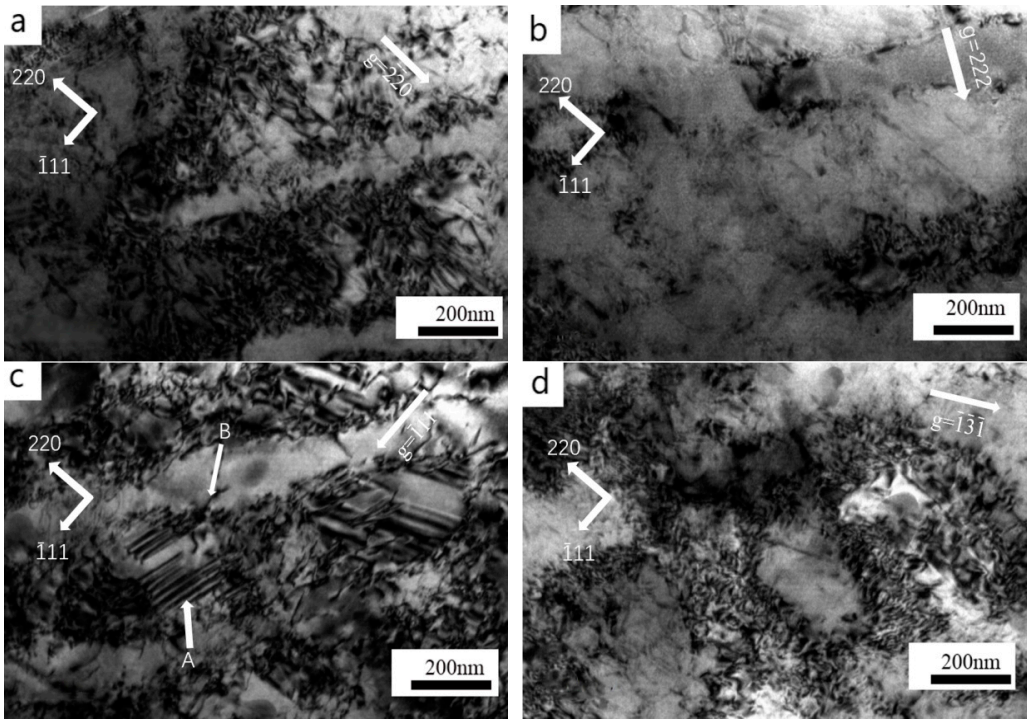


Figure 9. Dislocation configuration of 1Nb alloy after compression: (**a**) two-beam condition, with g = $\bar{2}\bar{2}0$; (**b**) g = $\bar{3}\bar{1}1$; (**c**) g = $\bar{1}11$; (**d**) g = $\bar{1}3\bar{1}$.

Suzuki A. et al. have shown that the addition of different elements to alloys will change the elemental distributions between the γ/γ′ phases and their lattice mismatch, further affecting the morphology of the γ′ particle and thereby modifying the mechanical properties of alloys [6,27]. Previous studies have reported that the strength of an alloy is related to the degree of mismatch, the volume fraction, and the size of the γ′ phase [28–30]. Within a certain range, the larger the mismatch, the greater the yield strength of the alloy, similar to nickel-based alloys. As seen in Table 2, as the Nb content increases, the mismatch also rises; so, the mismatch of the 3Nb alloy is the highest, which is 0.86%. However, the dimension of the γ′ precipitate of the 3Nb alloy is only 189 nm, which is the minimum among the five alloys. But it can be seen from Figure 1 that there are more Co_3V phases in the 3Nb alloy, which is a hard and brittle precipitation with an ordered close-packed hexagonal structure, so the presence of the Co_3V phase may also contribute to the strength of the 3Nb alloy, but the phase usually precipitates in the form of flakes, which facilitates the formation and propagation of cracks; the close-packed hexagonal structure has a reduced slip system, which is detrimental to the plasticity of the material, so it is not desirable to enhance the strength of the material by introducing large volumes of Co_3V. The yield strength of the 3Nb alloy is the largest among the five alloys, reaching 496 MPa. It has been proven that when the lattice mismatch between γ and γ′ is near 0, the γ′ precipitate is spherical in shape. If the mismatch of the dual phases is 0.5% ~ 1%, the γ′ particle is cuboidal; the mismatch of the five alloys is about 0.8%. Figure 5 shows that the morphology

of the γ′ phase is typically cubical. Figure 6 shows that Ti, V, and Nb are γ′ formers. The addition of γ′-former elements in the alloys enhances the volume ratio of the γ′ particle, so it can be concluded that the volume fraction of the γ′ phase increases slightly with the rise in Nb content.

After the alloys are compressed at 900 °C, the dimension of the γ′ phase in the alloys rises, while the volume ratio of the γ′ phase drops substantially. This may be due to the dissolution of some γ′ precipitates during cutting by the dislocations at high temperatures. Suzuki studied the compressive deformation mechanism of Co-Al-W alloys and found the following: (i) shearing of the γ′ phases by pairs of ½<110>-type perfect dislocations on {111} planes at low temperatures (293–978 K), (ii) at intermediate temperatures (around 1033 K), deformation by shearing of γ′ particles by the <112> {111} slide system, and (iii) cutting of the γ′ phases by <112> dislocations with the formation of stacking faults (above 1088K) [27]. In this study, after the Co-6Ti-11V alloy was compressed at 900 °C, the [101]-type compact dislocations cut the γ′ precipitate along the {111} plane, and two kinds of deformation mechanisms appeared in the Co-6Ti-11V-1Nb alloy, including $[1\bar{1}0]$ dislocations at the interface of γ/γ′ reacting to produce $[1\bar{2}1]$ partial dislocations, with the latter cutting the γ′ particle and forming SISFs. The reaction [20] is as follows:

$$1/2\ [0\bar{1}\ 1] + \rightarrow 1/3\ [1\bar{2}\ 1] + 1/6\ [\bar{1}\bar{1}2] + \text{SISF} \quad (4)$$

In summary, the dislocation motion of the 1Nb alloy deviates from that of the base alloy because there is no formation of stacking faults in the base alloy, while in the 1Nb alloy, the $[1\bar{1}0]$ dislocation reacts at the frontier of the γ/γ′ phases to form a 1/3 <$1\bar{2}1$> partial dislocation, which then shears the γ′ phase and forms stacking faults. These can be related to Nb reducing the energy stacking fault of Co-based alloys [31].

The addition of Nb in the Co-Ti-V ternary alloy is desirable, as it improves the phase stability of the γ′ phases, as well as enhancing the volume fraction of this precipitate. Consequently, this improves the mechanical properties of the alloys at elevated temperatures. However, the addition should be within 1 at. %.

4. Conclusions

1. After solution treatment at 1100 °C/48 h and aging treatment at 870 °C/72 h, for the alloys containing less than 1Nb, they show a γ and γ′ dual-phase microstructure and are free of deleterious phases. The Co_3V phase with a platelet shape is present in the 2Nb and 3Nb alloys.
2. With the increase in Nb content, the lattice mismatch of the γ/γ′ two-phase microstructure increases gradually. After compression at 900 °C, the size of the γ′ phase in the 0Nb alloy increases from 222.2 nm to 271.7 nm; the volume ratio of the γ′ phase in the three investigated alloys decrease gradually. The 1Nb alloy shows the minimum size increase and the smallest volume drop of the γ′ precipitate. These results show that Nb improves the phase stability of the γ′ phase.
3. The yield strength of the Co-Ti-V alloy increases with the increase in Nb content, and the yield strength of the 3Nb alloy is the highest when compressed at 900 °C, at 496 Pa.
4. When compressed at 900 °C, the <101>-type dislocation causing shearing of the γ′ phase in the {111} plane in the Nb-free alloy was observed. For the 1Nb alloy, some <$1\bar{1}0$> dislocations reacted at the γ/γ′ interface to generate 1/3 $[1\bar{2}1]$, and then the γ′ precipitate was cut by this dislocation, leaving R = <$\bar{1}21$> stacking faults.

Author Contributions: Data curation, S.N., E.L. and K.L.; writing—original draft, P.Z. and W.Z.; writing—review and editing, S.C. and Y.Q. All authors have read and agreed to the published version of the manuscript.

Funding: This research was financially supported by the National Key R&D Program of China [2021YFC2202402] and the National Natural Science Foundation of China (52275339, 51471079). The authors would also like to acknowledge funding support from the Undergraduate Innovation Program of JUST.

Institutional Review Board Statement: Not applicable.

Informed Consent Statement: Not applicable.

Data Availability Statement: The data are contained within the article.

Conflicts of Interest: Authors Wanxiang Zhao and Kunjie Luo are employed by the Suzhou Nuclear Power Research Institute. The remaining authors declare that the research was conducted in the absence of any commercial or financial relationships that could be construed as potential conflicts of interest.

References

1. Donachie, M.; Donachie, S. *Superalloys: A Technical Guide*, 2nd ed.; ASM International: Novelty, OH, USA, 2002; p. 439.
2. Sato, J.; Omori, T.; Oikawa, K.; Ohnuma, I.; Kainuma, R.; Ishida, K. Cobalt-base high-temperature alloys. *Science* **2006**, *312*, 90–91. [CrossRef] [PubMed]
3. Sims, C.T. A contemporary view of cobalt-base alloys. *J. Met.* **1969**, *21*, 27–42. [CrossRef]
4. Pollock, T.M. Alloy design for aircraft engines. *Nat. Mater.* **2016**, *15*, 809–815. [CrossRef]
5. Reed, R.C. *The Superalloys: Fundamentals and Applications*; Cambridge University Press: Cambridge, UK, 2006.
6. Suzuki, A.; Inui, H.; Pollock, T.M. L12-Strengthened Cobalt-Base Superalloys. *Annu. Rev. Mater. Res.* **2015**, *45*, 345–368. [CrossRef]
7. Bocchini, P.J.; Sudbrack, C.K.; Noebe, R.D.; Dunand, D.C.; Seidman, D.N.; Northwestern Univ, E.I.L. Effects of titanium substitutions for aluminum and tungsten in Co-10Ni-9Al-9W (at%) superalloys. *Mater. Sci. Eng. A* **2017**, *705*, 122–132. [CrossRef]
8. Bocchini, P.J.; Sudbrack, C.K.; Sauza, D.J.; Noebe, R.D.; Seidman, D.N.; Dunand, D.C.; Northwestern Univ, E.I.L. Effect of tungsten concentration on microstructures of Co-10Ni-6Al-(0,2,4,6)W-6Ti (at%) cobalt-based superalloys. *Mater. Sci. Eng. A* **2017**, *700*, 481–486. [CrossRef]
9. Ooshima, M.; Tanaka, K.; Okamoto, N.L.; Kishida, K.; Inui, H. Effects of quaternary alloying elements on the γ' solvus temperature of Co-Al-W based alloys with fcc/L12 two-phase microstructures. *J. Alloys Compd.* **2010**, *508*, 71–78. [CrossRef]
10. Pyczak, F.; Bauer, A.; GöKen, M.; Lorenz, U.; Neumeier, S.; Oehring, M.; Paul, J.; Schell, N.; Schreyer, A.; Stark, A.; et al. The effect of tungsten content on the properties of L12-hardened Co–Al–W alloys. *J. Alloys Compd.* **2015**, *632*, 110–115. [CrossRef]
11. Davydov, A.V.; Kattner, U.R.; Josell, D.; Waterstrat, R.M.; Boettinger, W.J.; Blendell, J.E.; Shapiro, A.J. Determination of the CoTi congruent melting point and thermodynamic reassessment of the Co-Ti system. *Metall. Mater. Trans. A* **2001**, *32*, 2175–2186. [CrossRef]
12. Liu, Y.; Takasugi, T.; Izumi, O. Alloying behavior of Co_3Ti. *Metall. Trans. A* **1986**, *17*, 1433–1439. [CrossRef]
13. Ruan, J.J.; Wang, C.P.; Zhao, C.C.; Yang, S.Y.; Yang, T.; Liu, X.J. Experimental investigation of phase equilibria and microstructure in the Co–Ti–V ternary system. *Intermetallics* **2014**, *49*, 121–131. [CrossRef]
14. Ruan, J.J.; Wang, C.P.; Yang, S.Y.; Omori, T.; Yang, T.; Kimura, Y.; Liu, X.J.; Kainuma, R.; Ishida, K. Experimental investigations of microstructures and phase equilibria in the Co–V–Ta ternary system. *J. Alloys Compd.* **2016**, *664*, 141–148. [CrossRef]
15. Zhou, G.J.; Tang, J.G.; Zhou, Y.; An, W.K.; Cai, A.H. Phase equilibria in the Co-Ti-V system at 873 K. *J. Alloys Compd.* **2014**, *602*, 49–52. [CrossRef]
16. Zhang, J.; Du, Y.; Liu, Y.; Zhang, W.; Liu, D.; Chen, C. Assessment of atomic mobilities for fcc Co-Ti-V alloys. *Calphad* **2018**, *61*, 179–188. [CrossRef]
17. Verma, S.K.; Pramanik, A.; Jyothsna, K.; Vamsi, K.V.; Karthikeyan, S. Phase transformation temperatures, γ–γ' lattice parameter misfit, and γ' precipitate morphology in Co–Ti–V alloys. *Metall. Mater. Trans. A* **2022**, *53*, 4011–4022. [CrossRef]
18. Ruan, J.J.; Liu, X.J.; Yang, S.Y.; Xu, W.W.; Omori, T.; Yang, T.; Deng, B.; Jiang, H.X.; Wang, C.P.; Kainuma, R.; et al. Novel Co-Ti-V-base superalloys reinforced by L12-ordered γ' phase. *Intermetallics* **2018**, *92*, 126–132. [CrossRef]
19. Zhou, P.; Gao, X.; Song, D.; Liu, Y.; Cheng, J. Effect of Ni on Microstructure and Mechanical Property of a Co-Ti-V-Based Superalloy. *Scanning* **2021**, *2021*, 678085. [CrossRef]
20. Zhou, P.; Gao, X.; Song, D.; Liu, Q.; Liu, Y.; Cheng, J. Role of Ru on the microstructure and property of novel Co-Ti-V Superalloy. *J. Mater. Res.* **2020**, *35*, 2737–2745. [CrossRef]
21. Liu, X.; Pan, Y.; Chen, Y.; Han, J.; Yang, S.; Ruan, J.; Wang, C.; Yang, Y.; Li, Y. Effects of Nb and W Additions on the Microstructures and Mechanical Properties of Novel gamma/gamma′ Co-V-Ti-Based Superalloys. *Metals* **2018**, *8*, 563. [CrossRef]
22. Xu, Y.; Xia, T.; Yan, J. Effect of alloying elements to hot corrosion behavior of novel Co-Al-W superalloy. *J. Chin. Soc. Corros. Prot.* **2010**, *30*, 457–464.

23. Migas, D.; Moskal, G.; Niemiec, D. Surface Condition of New γ–γ' Co-Al-Mo-Nb and Co-Al-W Cobalt-Based Superalloys After Oxidation at 800 °C. *J. Mater. Eng. Perform.* **2018**, *27*, 447–456. [CrossRef]
24. Klein, L.; Bauer, A.; Neumeier, S.; Göken, M.; Virtanen, S. High temperature oxidation of γ/γ'-strengthened Co-base superalloys. *Corros. Sci.* **2011**, *53*, 2027–2034. [CrossRef]
25. Makineni, S.K.; Nithin, B.; Chattopadhyay, K. Synthesis of a new tungsten-free γ–γ' cobalt-based superalloy by tuning alloying additions. *Acta Mater.* **2015**, *85*, 85–94. [CrossRef]
26. Takasugi, T.; Honjo, H.; Kaneno, Y.; Inoue, H. Plastic flow instabilities of $L1_2Co_3Ti$ alloys at intermediate temperatures. *Acta Mater.* **2002**, *50*, 847–855. [CrossRef]
27. Suzuki, A.; DeNolf, G.C.; Pollock, T.M. Flow stress anomalies in γ/γ' two-phase Co–Al–W-base alloys. *Scr. Mater.* **2007**, *56*, 385–388. [CrossRef]
28. Carroll, L.J.; Feng, Q.; Pollock, T.M. Interfacial Dislocation Networks and Creep in Directional Coarsened Ru-Containing Nickel-Base Single-Crystal Superalloys. *Metall. Mater. Trans. A* **2008**, *39*, 1290–1307. [CrossRef]
29. Zhang, J.X.; Murakumo, T.; Harada, H.; Koizumi, Y. Dependence of creep strength on the interfacial dislocations in a fourth generation SC superalloy TMS-138. *Scr. Mater.* **2003**, *48*, 287–293. [CrossRef]
30. Zhang, J.X.; Koizumi, Y.; Kobayashi, T.; Murakumo, T.; Harada, H. Strengthening by γ/γ' interfacial dislocation networks in TMS-162—Toward a fifth-generation single-crystal superalloy. *Metall. Mater. Trans. A* **2004**, *35*, 1911–1914. [CrossRef]
31. Lilensten, L.; Antonov, S.; Gault, B.; Tin, S.; Kontis, P. Enhanced creep performance in a polycrystalline superalloy driven by atomic-scale phase transformation along planar faults. *Acta Mater.* **2021**, *202*, 232–242. [CrossRef]

Disclaimer/Publisher's Note: The statements, opinions and data contained in all publications are solely those of the individual author(s) and contributor(s) and not of MDPI and/or the editor(s). MDPI and/or the editor(s) disclaim responsibility for any injury to people or property resulting from any ideas, methods, instructions or products referred to in the content.